J. Fluid Mech. (2024), *vol*. 997, A74, doi:10.1017/jfm.2024.794

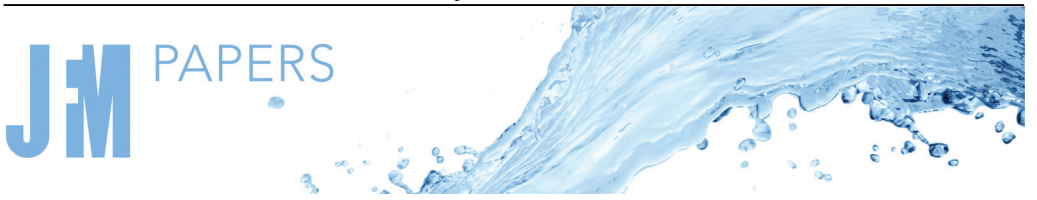

Gravity-driven flow of liquid bridges between vertical fibres

Chase T. Gabbard[1] **and Joshua B. Bostwick**[1],†

[1]Department of Mechanical Engineering, Clemson University, Clemson, SC 29631, USA

(Received 12 October 2023; revised 7 July 2024; accepted 7 July 2024)

Liquid bridges are formed when a flowing liquid interacts with multiple parallel fibres, as relevant to heat and mass transfer applications that utilize flow down fibre arrays. We perform a comprehensive experimental study of flowing liquid bridges between two vertical fibres whose spacing is controlled dynamically in our experimental apparatus. The bridge patterns exhibit a regular periodic spacing typical of absolute instability for low flow rates, but become spatially inhomogeneous above a critical flow rate where the base flow is convectively unstable. The shapes of individual bridges and their associated dynamics are measured, as they depend upon the liquid properties, and fibre geometry/spacing. The bridge length scales similarly to static bridges between parallel fibres. The bridge dynamics exhibits a dependence on viscosity and scale with the impedance. A simple energy balance is used to derive a scaling relationship for the bridge velocity that captures the general trend of our experimental data. Finally, we demonstrate that these scalings similarly apply when the fibres are dynamically separated or brought together.

Key words: liquid bridges, thin films, pattern formation

1. Introduction

Bead-on-fibre patterns form in liquids flowing down a fibre due to hydrodynamic instabilities, such as the Kapitza (Ter Haar 2016) and Plateau–Rayleigh (Plateau 1873; Rayleigh 1878) instabilities. Such flows have received increased attention over the past decade, in part due to nature's nifty use of bead-on-fibre structures for water harvesting and transport (Zheng *et al.* 2010; Ju *et al.* 2012; Xue *et al.* 2014; Guo & Tang 2015), and our attempts to imitate it may help to curb the anticipated global water crisis (Shi *et al.* 2018;

† Email address for correspondence: jbostwi@clemson.edu

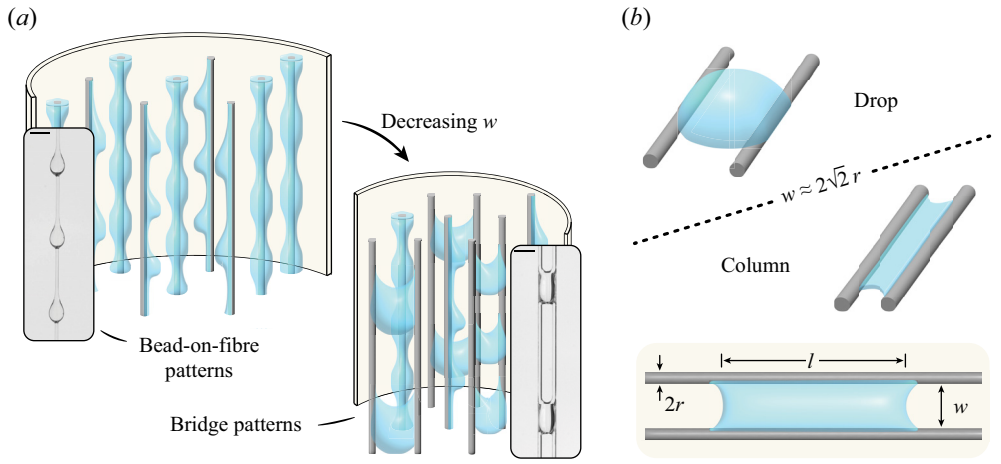

Figure 1. Liquids between fibres. (*a*) Schematic of flow down a fibre array showing bead-on-fibre patterns when the fibre spacing is large, and interactions between adjacent fibres when the fibre spacing is small, resulting in a mix of traditional bead-on-fibre patterns and bridge patterns. Inset images show associated bead-on-fibre and bridge patterns with a 3 mm scale bar. (*b*) A small liquid volume suspended between two parallel fibres of radius r can take on a rounded drop-like shape that transitions to a thin column shape as the fibre gap approaches $w \approx 2\sqrt{2}\,r$ (Protiere, Duprat & Stone 2013). The dimensions of the fibre radius r and gap w determine the length of the liquid profile ℓ for a given volume V.

Sadeghpour *et al.* 2019; Zeng, Sadeghpour & Ju 2019; Moncuquet *et al.* 2022; Jin *et al.* 2023). These high surface area flows are suitable for numerous heat and mass transfer applications, including heat exchange (Zeng *et al.* 2017), particle capture (Sadeghpour *et al.* 2021), aerosol capture (Labbé & Duprat 2019) and gas absorption (Chinju, Uchiyama & Mori 2000; Migita, Soga & Mori 2005). In practice, optimizing mass and heat transfer requires parallelization through large vertical fibre arrays whose size is often constrained by the system geometry (cf. figure 1*a*). Recent investigations have explored the role of fibre spacing in determining the critical fibre density where isolated bead-on-fibre patterns are formed (Wagstaff *et al.* 2023) and how this compares to a structured packing with the same dimensions (Zeng *et al.* 2017), in the context of wet scrubbers. When the fibres are closely spaced, the beads can interact with adjacent fibres forming flowing liquid bridges, as shown in figure 1(*a*). In this study, we present an experimental investigation of liquid bridges flowing between vertical fibres, aiming to contribute to the existing literature by elucidating the role of a base flow on bridge shape and dynamics.

Early studies on liquid–fibre interactions were motivated by textile applications (Minor *et al.* 1959; Kissa 1981; Kawase *et al.* 1986; Chen *et al.* 2001; Patnaik *et al.* 2006). In this context, Princen (1970) provided a detailed mathematical treatment for the equilibrium configuration of liquid confined between parallel fibres. Princen observed the existence of two states: (1) a rounded drop profile; and (2) a column profile that is convex outwards, extends further along the fibres, and is well predicted by his theoretical formulation. These two states are shown in figure 1(*b*). A number of recent investigations have focused on the transition between these two equilibrium states. For example, the wettability of the two parallel fibres was considered by Lukáš *et al.* (2006), who determined the transition criteria for complete wetting, partial wetting and super-hydrophobic surfaces, and reported hysteretic behaviour, which was later explored in detail by Wang & Schiller (2021) using lattice Boltzmann simulations.

Protiere *et al.* (2013) determined empirically the transition point between the drop and column profile, and showed that it depends critically upon the volume V, fibre gap w, and fibre radius r. They showed that when the volume of liquid is small ($V/r^3 < 700$), the transition point is $w = 2\sqrt{2}\,r$. However, both states can exist for large volumes. Additionally, they derived a scaling law for the bridge length by considering the relevant variables $\ell = f(w, V, r)$ and obtaining three dimensionless groups $\ell/r = f(w/r, V/r^3)$ governing the problem. They recognized the intuitive dependence of ℓ on V, and defined a composite parameter $(\ell/r)/(V/r^3) = \ell r^2/V$, similar to that defined previously by Duprat *et al.* (2012), which explained their experimental data. Their experimental results showed $\ell r^2/V \sim w/r$. Additional works have addressed more realistic scenarios observable in nature, namely elastic and non-parallel fibres. Duprat *et al.* (2012) explored the shape transition and elastocapillary adhesion of drops between flexible fibres, showing that the drop could spread completely, partially or not at all, and that this distinction depends upon the drop volume and fibre geometry and wetting properties. Furthermore, varying the tension of flexible parallel fibres can 'zip' them together or cause the breakup of the liquid drop (Duprat & Protiere 2015). Fibres with dissimilar radii (Sauret *et al.* 2015*a*) and random orientation (Sauret *et al.* 2015*b*) have also been considered and compared with the theoretical and experimental results for equivalent and parallel fibres (Princen 1970; Protiere *et al.* 2013).

The results above provide physical insight into the static equilibrium shape of a liquid between parallel fibres. The literature on the dynamics of liquids between parallel fibres is comparatively sparse and mostly limited to the extensional dynamics of liquid bridges, which are useful for characterizing viscoelastic fluid properties through thinning and breakup (Sridhar *et al.* 1991; Entov & Hinch 1997), and have wide-ranging industrial and biological applications, as reviewed by Montanero & Ponce-Torres (2020). Furthermore, the capillary and viscous forces associated with bridges in extension have been explored (Pitois, Moucheront & Chateau 2000), and viscosity has been shown to play a critical role in bridge rupture (Mazzone, Tardos & Pfeffer 1987). To our knowledge, the addition of a base flow to the drop between fibres system has yet to be explored. The shear dynamics of bridges is relevant to numerous heat and mass transfer applications mentioned earlier, as well as more traditional processes such as fibre coating (Quéré 1999), where liquid bridging fibres leads to partially coated and uneven surfaces. For example, Kurtyigit *et al.* (2023) showed the potential for static bridges in a cross-flow to capture particles. However, a base flow, which is essential for transporting the particle-laden bridges, has not been considered. The dynamics of beads on fibres is affected by base flow stability, resulting in bead patterns and interactions (Kliakhandler, Davis & Bankoff 2001; Duprat *et al.* 2007), as well as film-mediated and aerodynamic interactions that can spatially orient beads along a fibre (Duprat *et al.* 2009) and across multiple parallel fibres (Wilson *et al.* 2023), respectively. Here, we present an experimental study of flowing bridge patterns driven by gravity that introduce inertial and viscous forces that were unimportant in the previous work on the equilibrium shape between fibres (Protiere *et al.* 2013).

We begin this paper by describing the experimental apparatus and protocol that we used to create flowing liquid bridges between parallel fibres, as well as the image processing techniques that define the dynamic liquid bridge properties, as discussed in § 2. In § 3, we describe the formation of bridge-between-fibre patterns, and identify the conditions under which steady patterns emerge. Our experimental results are presented in § 4 and highlight how different experimental parameters impact the bridge pattern, as well as the shape and speed of individual bridges. We also show how the bridge geometry can be controlled

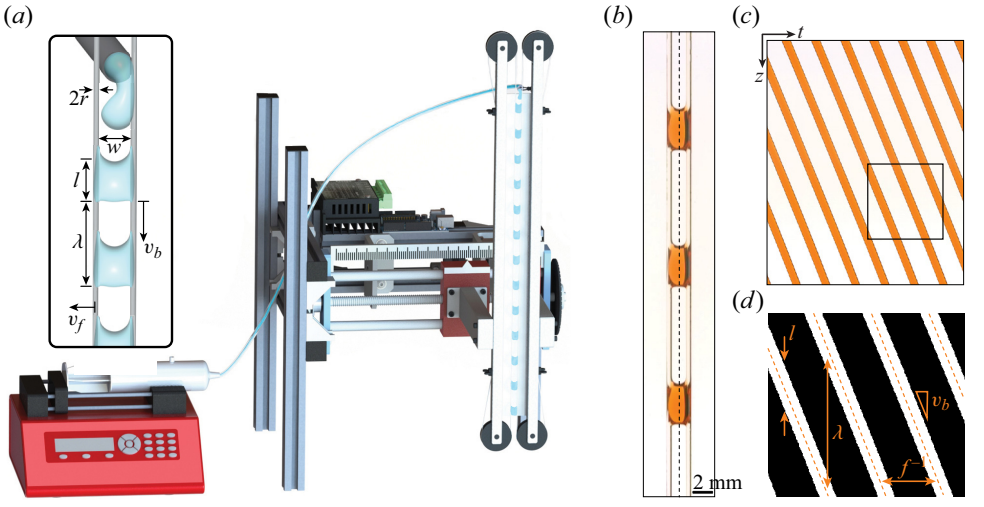

Figure 2. Experimental set-up and image analysis. (*a*) A syringe pump delivers a controlled flow to two vertical fibres, spaced at distance w apart, and adjusted using a custom linear actuator. The inset illustrates a typical bridge pattern with associated experimental variables. (*b*) A bridge pattern with midline shown as the black dashed line is used to create (*c*) a spatiotemporal diagram that demonstrates both uniform spacing and steady dynamics. (*d*) A binarized section (with liquid white) of the spatiotemporal diagram (black box in *c*) shows the variable measurements (ℓ, λ, f, v_b).

using dynamic fibres. We offer concluding remarks in § 5, and provide recommendations for future research directions and potential applications of thin film flow between fibres.

2. Experiment

Flowing liquid bridges were created using the experimental set-up in figure 2. A linear actuator driven by an Arduino-controlled stepper motor was used to dynamically control the spacing w between two vertical fibres. A microstep driver and vibration dampeners were used so the fibres could be displaced smoothly for speeds between $0.01\,\mathrm{mm\,s^{-1}}$ and $4\,\mathrm{mm\,s^{-1}}$. The fibres were nylon monofilament with radius $0.15\,\mathrm{mm} \leq r \leq 0.95\,\mathrm{mm}$, tightened with inline tensioners to eliminate deformation-induced spreading (Duprat & Protiere 2015) and fibre entanglement (Shi *et al.* 2020). An NE-1000 syringe pump was used to apply a flow rate Q through a stainless steel nozzle of diameter r_n onto the side of a fibre that could interact with the neighbouring fibre while destabilizing. The resulting bridge patterns were captured using a Phantom VEO-410L high-speed camera at a position 400 mm below the nozzle – a sufficient distance for capturing steady-state dynamics. An LED panel was used as a backlight for all experiments.

Glycerol–water mixtures and silicone oil were used as the working fluids, which provided a viscosity range $\mu = 9.5$–$699\,\mathrm{mPa\cdot s}$, surface tension range $\sigma = 21.1$–$62.7\,\mathrm{mN\,m^{-1}}$, and density range $\rho = 969$–$1250\,\mathrm{kg\,m^{-3}}$. The viscosity was measured using a cone–plate shear rheometer (Anton Paar MCR 302), and the surface tension and density were measured using an Attension Sigma 702 force tensiometer with a Wilhelmy plate and density probe, respectively. Glycerol–water mixtures were used as our primary working fluids because of their tunable viscosity and high surface tension, which was critical to produce large asymmetric beads that could interact with a neighbouring fibre at large w (Gabbard & Bostwick 2021*a*). The contact angle between the glycerol–water

mixtures and nylon fibres was $\phi = 65^\circ \pm 9.3^\circ$, measured optically using the largest fibre $r = 0.95$ mm. To capture wettability effects, we also tested silicone oils with symmetric bead profiles for all r, limiting the range of interfibre spacing to $w \leq 1.5$ mm (Wagstaff *et al.* 2023). The relevant dimensionless parameters include the Reynolds number $Re \equiv \rho v_b w/\mu \sim 10^{-3}$–$10^{-1}$ and Weber number $We \equiv \rho v_b^2 w/\sigma \sim 10^{-4}$–$10^{1}$, indicating that viscous and capillary forces both dominate inertial forces for the majority of tests. The role of inertia may also be compared to gravity by comparing $F_g/w^2 = \rho g V/w^2$ with the dynamic pressure $p_d \sim \rho v_b^2$, which shows a negligible role of inertia when $v_b w/\sqrt{gV} \leq 1$. This holds true for all experiments. The dominant role of viscosity and capillarity over inertia leads us to also define the capillary number $Ca \equiv v_b \mu/\sigma \sim 10^{-2}$–$10^{-1}$. Finally, we define the Bond number $Bo \equiv \rho g w^2/\sigma \sim 10^{-1}$–$10^{0}$. Herein, the Bond number plays a critical role in this gravity-driven capillary phenomena where the maximum w that we could test for each liquid corresponds to $Bo \approx 1$, or $\ell_c \approx w$, where $\ell_c = \sqrt{\sigma/\rho g}$ is the capillary length.

Each experiment began by attaching and tensioning two dry fibres to the linear actuator. The fibres were slowly brought together until they touched and then separated by a user-defined distance w. The nozzle was oriented perpendicular to the fibres and positioned carefully to touch a portion of one of the fibres but not the other. A flow rate Q was then applied by the syringe pump for several minutes to achieve a steady pattern, which was then imaged at 1000 f.p.s. The constant flow resulted in periodic bridge formation, which ensured that each bridge flowed at a constant velocity on the thin film deposited by the previous bridge. These steps were repeated for increasing Q until the flowing bridges began to interact at a critical flow rate $Q = Q_c$. All bridge patterns were qualitatively similar and exhibited a periodic structure and uniform motion within a flow rate range $Q_b \leq Q \leq Q_c$, which will be discussed in § 3.

We used MATLAB and ImageJ for image processing to extract the bridge properties defined in figure 2(*a*). A frame from a typical experiment is shown in figure 2(*b*). The dashed vertical line corresponds to the midpoint between the fibres. We construct the spatiotemporal diagram shown in figure 2(*c*) by tracking the pixel column associated with the midpoint with time. The orange diagonal lines correspond to the liquid bridge, where the lines' negative slope indicates downward motion. Additionally, the constant slope and the even spacing between diagonal lines indicate that the bridges move at a constant velocity and spacing – permitting easy data acquisition from the spatiotemporal diagram. A small region of the spatiotemporal diagram is binarized and displayed in figure 2(*d*) with the measurements extracted during image processing overlaid. These values are taken for the full spatiotemporal diagram, and their mean and standard deviation are used for the final value and error of each experiment. The average bridge volume is $V = Q/f$.

3. Phenomenology: forming the bridge pattern

Depositing a drop of non-volatile liquid with known volume between two fibres is straightforward using a pipette. However, creating dynamic liquid bridges of known volume is more challenging: a dynamic bridge sliding down two fibres will lose mass as it coats the fibres, resulting in a non-constant size and speed. We circumvent this complexity by forming a series of flowing bridges that (i) have nearly identical volumes due to their periodic genesis, and (ii) do not change volume since they flow on the film deposited by the previous bridge. These periodic bridges result from capillary instability of the flow along a single fibre. The initial bead-on-fibre patterns grow in the transient region near

the nozzle, and interact with the neighbouring nozzle periodically, thereby restructuring the bead-on-fibre pattern into a bridge-between-fibres pattern, as shown in movie 1 of the supplementary material, available at https://doi.org/10.1017/jfm.2024.794. We note that this method faithfully reproduces the patterns that may arise in fibre arrays with high fibre density – a scenario especially relevant for patterns that are not symmetric about the fibre (Gabbard & Bostwick 2021*a*, 2023*a*; Eghbali *et al.* 2022; Cazaubiel & Carlson 2023).

Figure 3(*a*) plots bridge frequency f (red, left-hand axis) and bridge volume V (blue, right-hand axis) against flow rate Q. As flow rate Q increases, bridge frequency f increases monotonically until a critical flow rate Q_c, beyond which the bridges interact, resulting in a stark increase in frequency variability. These interactions result from mass differences in the bridges that originate from a convectively unstable base flow in the initial coating on a single fibre, which causes growing beads to interact before forming bridges of different mass. Consequently, all data points associated with flow rates exceeding Q_c have been excluded from this study. Movie 2 of the supplementary material shows a typical coalescence event. For low flow rates $Q < Q_b$, the film deposited by a bridge destabilizes into a bead-on-fibre pattern before the subsequent bridge arrives. The destabilization is due to the Plateau–Rayleigh instability and has a typical time scale $\tau_{PR} = 3\mu r^4/\sigma h_0^3$, where h_0 is the uniform coating of the base flow (Gallaire & Brun 2017). Thus film breakup occurs when $\tau_{bridge} > \tau_{PR}$ or $f < \sigma h_0^3/3\mu R^4$. The overlaid experimental images show increased bridge density with Q and interacting bridges above Q_c. Despite the monotonic relationship between f and Q, the estimated bridge volume $V = Q/f$ exhibits non-monotonic behaviour as V achieves a local maximum before Q_c. This implies that a decrease in bridge size can be a precursor to the transition to convectively unstable flow, and is a sign of nonlinearity. This non-intuitive behaviour aligns with previous observations of thin film flow down a fibre (Gabbard & Bostwick 2021*b*). We note that while the bridge volume V depends upon the flow rate Q, its effect is minor. To achieve a larger range of V, the nozzle radius r_n is varied between 0.6 and 1.45 mm, resulting in a large range of bridge volumes, $V = 6.4$–$53\ \mathrm{mm}^3$.

Figure 3(*b*) shows the structure of a bridge pattern with film breakup $Q < Q_b$. The beads seen below the downward flowing bridge cause two undesired oscillations in the bridge properties: (i) the bridge length increases as it passes over beads, then decreases over the dry region; and (ii) since the beads on neighbouring fibres can be at different heights, the bridge can oscillate in the image plane. For $Q_b \leq Q \leq Q_c$, the bridges flow smoothly on a uniform film coating the fibres. Figure 3(*c*) shows the structure of the bridges that we explored. The two highlighted areas show close-up images of the meniscus connecting the front and back of the bridge with the thin film for glycerol–water mixtures, showing that no contact line is present – a feature that we will leverage to develop a simple model of the bridge dynamics. A comparison of each flow type and a close-up of the menisci connecting the bridge to the thin film coating the fibre are included in movies 3 and 4 of the supplementary material.

4. Results

We performed 1112 experiments over an extensive range of system geometry, including fibre radius r and interfibre spacing w, and liquid properties, including surface tension σ and viscosity μ. We quantify the bridge patterns through the bridge geometry ℓ, and bridge dynamics v_b, λ. We begin by showing the experimental bridge patterns and how

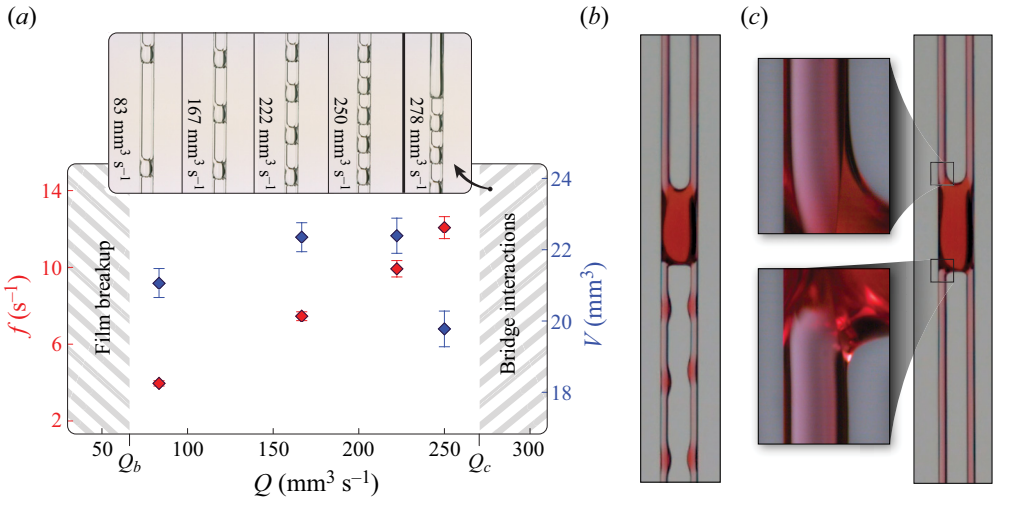

Figure 3. (*a*) Bridge frequency f (red, left-hand axis) and bridge volume V (blue, right-hand axis) plotted against flow rate Q, with inset images showing the bridge patterns. The shaded areas represent the data collection range: to the left, thin films between bridges destabilize due to the Plateau–Rayleigh instability; to the right, the shaded area and the inset's rightmost bridge pattern denote convectively unstable base flows. (*b*) At low flow rates, the bridge frequency is low, and the film between subsequent beads can break up. (*c*) When the frequency is sufficiently large to avoid film breakup, a steady bridge pattern forms and flows down the fibres on a uniform film. The highlighted areas indicate the meniscus linking the bulk fluid to the thin film on the fibres. For reference, the fibre radius is $r = 0.25$ mm.

the bridge length ℓ depends on the system parameters, comparing our findings with those for static bridges. We then show how the bridge velocity v_b depends upon the experimental parameters, including the viscosity over an order of magnitude. Finally, we set the fibres in motion and examine ℓ and v_b as they converge or diverge.

To begin, we show some typical qualitative trends observed in our data. Figure 4(*a*) shows how the liquid bridge shape changes with increasing fibre spacing w. Here, the bridge length ℓ decreases nonlinearly with increasing w, which is consistent with the behaviour expected for a static drop formed between two fibres (Protiere *et al.* 2013). A significant reduction in ℓ is particularly evident between the first two images, as this corresponds to the transition from a column-like shape to a drop-like shape for small w. As w increases further, the changes in ℓ become less pronounced until the bridges detach from one of the fibres, causing them to flow asymmetrically down a single fibre thereafter. Figure 4(*b*) shows how the liquid bridge shape changes with viscosity μ. Here, we note that viscosity has a negligible effect on ℓ, but does play a significant role in the dynamics, as we will discuss. For reference, we include the average bridge volume V in figures 4(*a*,*b*), as this implicitly affects the length ℓ.

Figure 4(*c*) plots bridge length ℓ against fibre spacing w for all experiments with $r = 0.25$ mm and $\mu = 90\,\text{mPa}\cdot\text{s}$. The colour bar correlates the marker colour with the estimated volume V of the bridge. Two key trends are observed: (i) ℓ decreases nonlinearly as w increases; and (ii) ℓ increases with volume, as shown by the transition from blue to red data markers as ℓ increases for constant w. The velocity v_b from the same set of experiments is shown in figure 4(*d*) against fibre spacing w. The velocity increases with w and shows a slight positive trend with V. These trends are typical of all experiments.

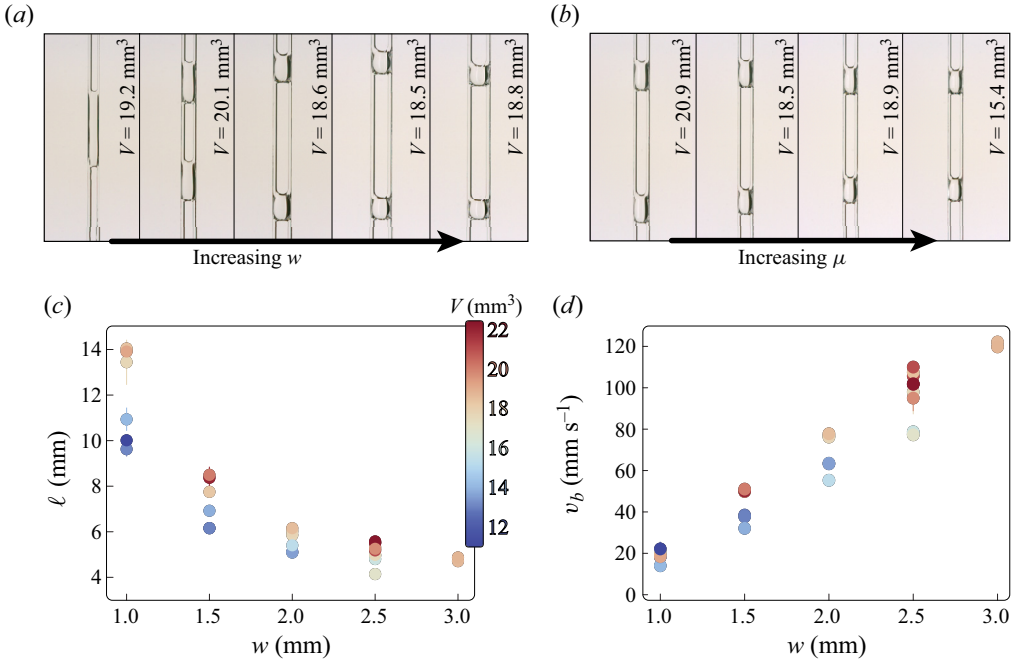

Figure 4. Bridge geometry. (*a*,*b*) Typical bridge profile for (*a*) increasing fibre gap w with fixed viscosity μ, and (*b*) increasing viscosity μ with fixed fibre gap w, both with $r_f = 0.25$ mm. (*c*) Bridge length ℓ and (*d*) velocity v_b against fibre gap w for bridge volume $11.5 \leq V \leq 22\,\text{mm}^3$, where the marker colour corresponds to the volume given in the colour bar. The fibre radius is $r = 0.25$ mm, and liquid viscosity is $\mu = 90\,\text{mPa}\cdot\text{s}$. Bridge length decreases nonlinearly as w increases, while bridge velocity increases with w and increases with V.

4.1. *Bridge shape*

The shape of the bridge between parallel fibres can take on a range of complex profiles with associated length ℓ, width w, and thickness h. The primary shape descriptor is ℓ, which is readily measurable and unbounded. We note that the bridge width is essentially determined by the user-defined fibre gap w and radius r, and any variations in thickness h are relatively small compared with changes in ℓ. As mentioned previously for the static case (Protiere *et al.* 2013), the bridge length varies significantly between the rounded drop state (small ℓ) and thin column state (large ℓ), with a sensitive transition region.

Since the bridge length ℓ depends on volume V, we express ℓ as a function of fibre gap w and volume V, and apply dimensional analysis with $V^{1/3}$ the characteristic length. We find that when r and σ are constant, $\ell/V^{1/3} \sim w/V^{1/3}$. Figure 5(*a*) plots $\ell/V^{1/3}$ against $w/V^{1/3}$ for a range of viscosities μ and fixed fibre radius $r_f = 0.25$ mm, showing a rapid decrease in ℓ with increasing w that approaches a horizontal asymptote as $w/V^{1/3} \to 1$. Note the vertical asymptote for small w, below which ℓ is too large to form bridge patterns and instead results in infinite or interacting columns. The data suggest $\ell = f(w)$. If we consider a bridge with constant volume $V = w\ell h$ and assume that changes in w alter ℓ such that $V/h = \ell w$ is constant, then an inverse relationship is expected. The dashed line in figure 5(*a*) shows the data fit to a curve of the form $\ell \sim 1/w$. The data fit the trend except at low w, where the transition from a column to drop occurs, and a swift change in bridge thickness is expected. Additionally, these results verify that μ plays a negligible role in the shape geometry.

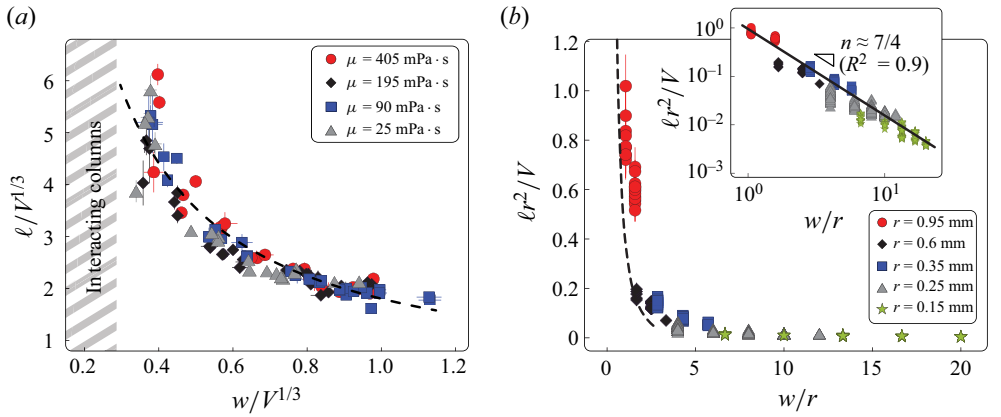

Figure 5. (*a*) Dimensionless bridge length $\ell/V^{1/3}$ plotted against dimensionless fibre gap $w/V^{1/3}$ as it depends upon the viscosity μ, for $r = 0.25$ mm. The dashed line fits the data to the scaling $\ell \sim 1/w$, expected for bridges with equal thickness. (*b*) Dimensionless bridge length $\ell r^2/V$ plotted against aspect ratio w/r for all data. The data collapse along a single trend that closely follows the Princen (1970) prediction for low aspect ratio (dashed line), and approaches a small, nearly constant value as aspect ratio increases. The inset shows the data plotted on a logarithmic scale and overlaid with a power-law fit (solid line) with power-law index $n \approx 7/4$ ($R^2 = 0.9$).

If we expand our analysis to include r, such that $\ell = f(w, V, r)$, then we arrive at the scaling law for static bridges between fibres given by Protiere *et al.* (2013) and discussed in § 1. We test this scaling in figure 5(*b*), which plots $\ell r^2/V$ against w/r for all experiments. The data markers indicate the fibre radius r. Our data follow a single trend and realize many of the same conclusions shown in figure 5(*a*). The data closely mirror those for static bridges, and show that this geometric scaling accurately captures the shape of flowing liquid bridges between fibres. The dashed line for small aspect ratio w/r corresponds to the analytical expression for a static liquid column between parallel fibres derived by Princen (1970) and compared favourably with static bridges by Protiere *et al.* (2013) for contact angle $\phi = 0^\circ$ (see (A1)–(A3)). The derivation can be found in Appendix A for reference. This predicted line is calculated for a contact angle $\phi = 0^\circ$, a convenient assumption validated by the thin film of the same fluid that the bridge flows along (cf. figure 3*c*). The inset re-plots the data on a logarithmic scale and fits the data to a power-law trend across several decades of dimensionless bridge length. The power-law index is $n \approx 7/4$, with $R^2 = 0.9$.

4.2. *Bridge dynamics*

The dynamics of flowing bridges is quantified by their velocity v_b, which is constant for patterns with $Q_b < Q < Q_c$. We begin with glycerol–water mixtures with fixed fibre size $r = 0.25$ mm, which suggests that $v_b = f(w, V, g)$, resulting in two dimensionless groups: $v_b/V^{1/6}g^{1/2}$ with $v_g = V^{1/6}g^{1/2}$ being the gravitational velocity scale, and $w/V^{1/3}$, where $V^{1/3}$ is the characteristic length. Figure 6(*a*) plots the dimensionless velocity $v_b/V^{1/3}g$ against the dimensionless fibre spacing $w/V^{1/3}$, as it depends upon viscosity μ, which reveals a power-law trend for each data set that shifts upwards with decreasing μ. This result suggests that $v_b/v_g = A(\mu)f(w/V^{1/3})$. We assume that $A(\mu)$ takes the form $1/\mu$, and re-plot the data in the inset. The collapse validates our assumption and provides a useful scaling when r is neglected.

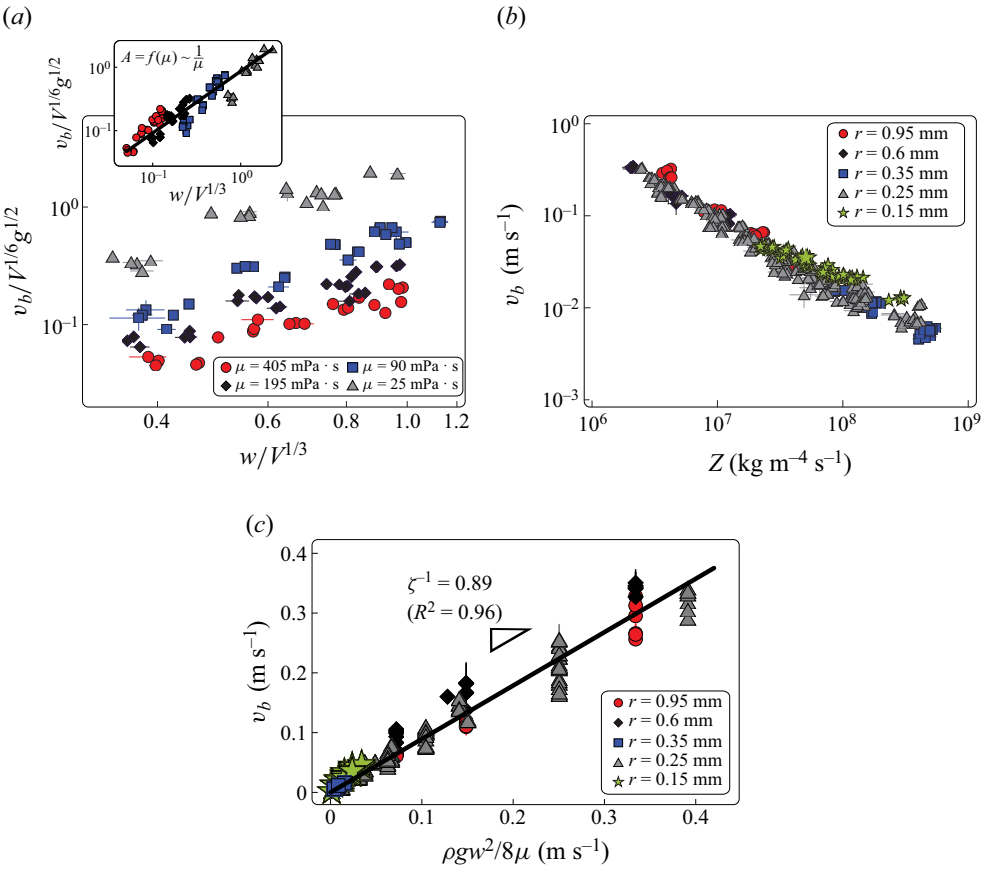

Figure 6. Bridge dynamics. (*a*) Dimensionless bridge velocity $v_b/V^{1/6}g^{1/2}$ against dimensionless fibre gap $w/V^{1/3}$ as it depends upon viscosity μ for all data with fibre radius $r = 0.25$ mm. The inset shows a power-law scaling (solid line) collapse of the data, with coefficient A as a function of μ, proportional to $1/\mu$, where A is the coefficient multiplying the independent variable. (*b*) Dimensional bridge velocity v_b against impedance $Z = \mu\ell/Vw$ as it depends upon the fibre radius r. (*c*) Bridge velocity against predicted velocity $v_p = \rho g w^2/8\mu$ for all experiments. The data trend linearly with the predicted velocity ($R^2 = 0.96$), and reveal a dissipation factor $\zeta = 1/0.89 \approx 1.12$.

Figure 4(*d*) revealed that v_b has a positive linear trend with w, and figure 6 shows that it is inversely proportional to μ. These observations form a basis for determining the viscous resistance or impedance Z as the viscous pressure per fluid volume velocity. Thus we need to estimate the cross-sectional area of the bridge, A_b. Letting $A_b = V/\ell$, we determine $Z = \mu\ell/Vw$. In figure 6(*b*), we plot v_b against Z, and note that our data collapse to a single trend, suggesting that the impedance is defined correctly for this system, and is the primary determinant of the bridge velocity. Although this is true across all fibre sizes and glycerol–water mixtures, this expression is not generalized, as it involves the comparison of dissimilar dimensional quantities. Despite this, it provides insight into how viscous dissipation influences the bridge velocity, and gives credence to our assumption that $A_b = V/\ell$.

Viscosity μ and bridge volume V play a critical role in determining the bridge velocity v_b, as shown in figure 6(*b*). This observation suggests that the velocity can be determined by balancing the viscous dissipation and gravity, particularly in situations where ℓ is small

and v_b is large. Neglecting capillary effects, the energy rates associated with potential gravitational energy and viscous dissipation in the bulk are

$$\Phi_g \approx \rho g V v_b, \tag{4.1a}$$

$$\Phi_\mu \approx \zeta 2\mu \left(\frac{\partial v}{\partial r}\right)^2 V. \tag{4.1b}$$

Here, ζ is an empirical coefficient associated with the dissipation, and $\partial v/\partial r$ is the shear rate, $\partial v/\partial r \approx 2v_b/w$. The rate balance becomes

$$\rho g V v_b = \zeta \frac{8\mu V v_b^2}{w^2}, \tag{4.2}$$

which gives a predictive scaling for the bridge velocity:

$$v_b \sim \frac{1}{\zeta}\frac{\rho g w^2}{8\mu}. \tag{4.3}$$

Figure 6(*c*) plots the bridge velocity v_b against the scaling defined in (4.3), showing a collapse of all experimental data onto the curve $v_b = 0.89(\rho g w^2/8\mu)$, with a high coefficient of determination ($R^2 = 0.96$), and suggesting an empirical dissipation factor $\zeta \approx 1.12$. We note that this model is accurate across practical ranges of w and r, as well as a large range of fluid properties (σ, μ, ρ).

4.3. *Bridges flowing between dynamic fibres*

We can actively control the bridge length and velocity by adjusting the separation distance $w = w(t)$. We explore this by forming a steady pattern of liquid bridges and then actuating one fibre, moving it towards or away from the other fibre at a velocity v_f. Figure 7(*a*) illustrates the two cases, where the fibres were brought together ($v_f < 0$) or separated ($v_f > 0$) at constant speed. The midline between the fibres was tracked over time and then converted to binary spatiotemporal diagrams for data extraction, as shown in figure 7(*b*). Here, the upper diagram shows the fibres converging, resulting in elongating bridges (white), and the lower diagram shows the fibres diverging until the bridges detach from one of the fibres. In order to determine the volume V inside the bridges, a steady pattern was first formed at a fixed w and used to determine the frequency, thereby yielding an estimate for V. At time $t = 0$ s, the fibre was set in motion, and the changes in bridge shape and speed were tracked.

In § 4.1, we found that the appropriate dimensionless form of the bridge length is $\ell r^2/V$. In figure 7(*c*), we plot the dimensionless bridge length against time t for fibre separation rates v_f ranging from $0.1\,\mathrm{mm\,s^{-1}}$ to $2\,\mathrm{mm\,s^{-1}}$. Since each test began with $w = 1$ mm, their initial lengths are similar; however, they evolve differently based on the v_f values. For higher v_f, the bridge length decreases faster and reaches its minimum value before detaching from a fibre more quickly, as indicated by the farthest right point along each data set. We note that a qualitative similarity exists between the trends and collapse upon re-plotting the data against aspect ratio w/r, as shown in the inset. Thus for the range of v_f tested, the velocity plays a minor role on the length of the bridge at a given w, and we can expect our previous scaling to hold. Figure 7(*d*) plots the dimensionless bridge length against aspect ratio w/r for all experiments with dynamic fibres. The blue and red data show the dimensionless length during fibre actuation for decreasing and increasing

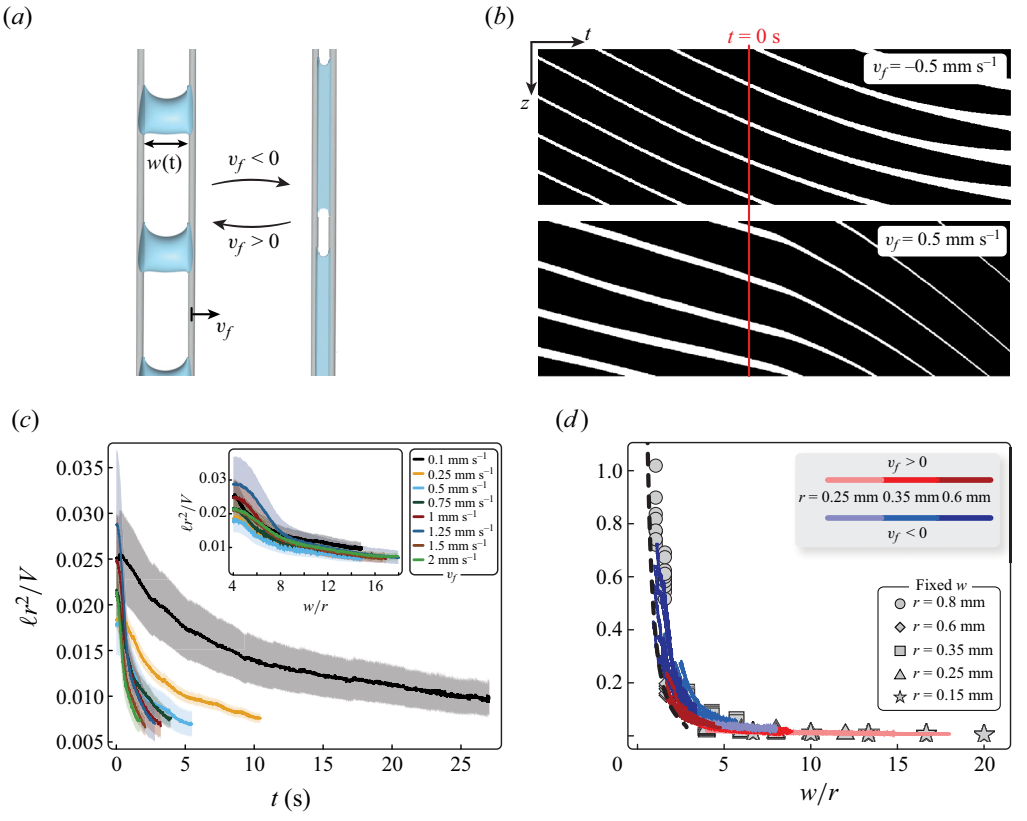

Figure 7. Geometry of a liquid bridge between dynamic fibres. (*a*) Schematic illustrating the two scenarios, with the fibres (1) being brought together at a constant velocity $v_f < 0$ (left to right), or (2) being separated at a constant velocity $v_f > 0$ (right to left). (*b*) Spatiotemporal diagram of the bridge pattern midline as the fibres are brought together (top) and separated (bottom) at 0.5 mm s^{-1}. The bridge pattern is established while the fibres are static, resulting in uniform white lines, and then evolves with time once the fibres begin actuating at $t = 0$ s, as marked by the vertical red line. (*c*) Dimensionless bridge length $\ell r^2/V$ against time t for fibres of size $r = 0.25$ mm separating at velocities $0.1 \leq v_f \leq 2$ mm s^{-1}. The inset shows the dimensionless bridge length against aspect ratio w/r. (*d*) Dimensionless bridge length $\ell r^2/V$ against aspect ratio w/r as the fibres were brought together (blue lines) or separated (red lines). Data from experiments with increasing fibre radius r are differentiated by progressively darker shades. Grey markers represent static-fibre test results, while the dashed line indicates the theoretical length (Princen 1970). Data from dynamic-fibre tests are consistent with static-fibre observations and theoretical predictions at low aspect ratios.

spacing, respectively. Three fibre radii were tested, and the coloured data are darkened to show increasing r. Additionally, three viscosities μ were used, ranging from 9.5 mPa · s to 699 mPa · s. The static-fibre data (grey markers) and theoretical curve from Princen (1970) from figure 5(*b*) are included, and show that the dynamic-fibre results directly overlay the static-fibre results. Thus we conclude that this scaling is appropriate even when the fibre spacing evolves, and holds for separation rates up to $v_f = 2$ mm s^{-1}.

Figure 8 plots the bridge velocity v_b against time t for the eight different separation rates v_f ranging from 0.1 mm s^{-1} to 2 mm s^{-1} for fibre radius $r = 0.25$ mm. As v_f increases, the velocity increases at a higher rate, leading to bridge detachment at smaller t. We again note the similarity among tests, and re-plot our data in terms of the fibre spacing w. Figure 8(*b*) shows v_b against the aspect ratio w/r for the tests shown in figure 8(*a*). Again, we see that

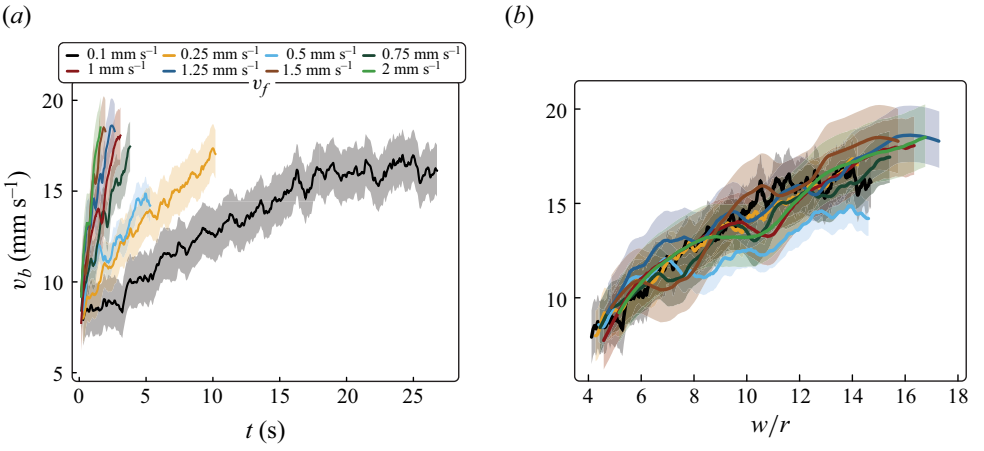

Figure 8. Bridge velocity between dynamic fibres. (*a*) Bridge velocity v_b against time t for fibres of size $r = 0.25$ mm separating at $0.1\,\mathrm{mm\,s^{-1}} \leq v_f \leq 2\,\mathrm{mm\,s^{-1}}$. (*b*) Bridge velocity v_b against aspect ratio w/r for the eight separation speeds detailed in (*a*). The trend of v_b with respect to w/r is invariant with respect to separation rate.

the data collapse along a single trend, irrespective of v_f. The trend is approximately linear, matching the empirically determined dependence of v_b on w. We therefore conclude that v_f plays a minor role in setting ℓ and v_b, rendering our conclusions from the static-fibre tests applicable for fibres converging or diverging at rate $2\,\mathrm{mm\,s^{-1}}$ or below. This demonstration of active control over shape and speed represents a novelty among liquid–fibre systems, and can be realized using actuators on individual fibres or using non-contact light-actuated materials (Bao *et al.* 2023).

5. Concluding remarks

In this study, we conducted an extensive experimental investigation of the shape and dynamics of flowing liquid bridges. We described a method for producing flowing bridge patterns, and elucidated the flow rate range associated with homogeneous bridge patterns. We discussed some of the general trends observed, namely that the bridge length ℓ is independent of viscosity but sensitive to changes in volume V and fibre spacing w. A dimensionless bridge length is defined following the work of Protiere *et al.* (2013), and scales with the aspect ratio w/r for all our experiments. We derived a simple model for the bridge velocity by balancing the driving gravitational force with viscous dissipation, which showed good agreement with our experimental data. Finally, we showed that our results are robust even when the fibres are mobile, such that scalings for the bridge length and bridge velocity are unaffected whenever the separation rate is $v < 2\,\mathrm{mm\,s^{-1}}$.

Our results provide valuable practical insights into recent advances in heat and mass transfer applications that utilize bead-on-fibre flows in fibre arrays. In these systems, unintentional flowing bridges can emerge due to optimizing fibre density in a constrained geometry. However, flowing bridges can also be desirable to optimize liquid–fibre systems. For instance, they can exhibit diverse shapes and speeds compared to conventional bead-on-fibre patterns, and mobile fibres can provide active control over bridge properties, as shown in figures 7 and 8. Furthermore, the use of liquid between actuated fibres has already shown the potential to transport and mix drops (Khattak *et al.* 2024). Our

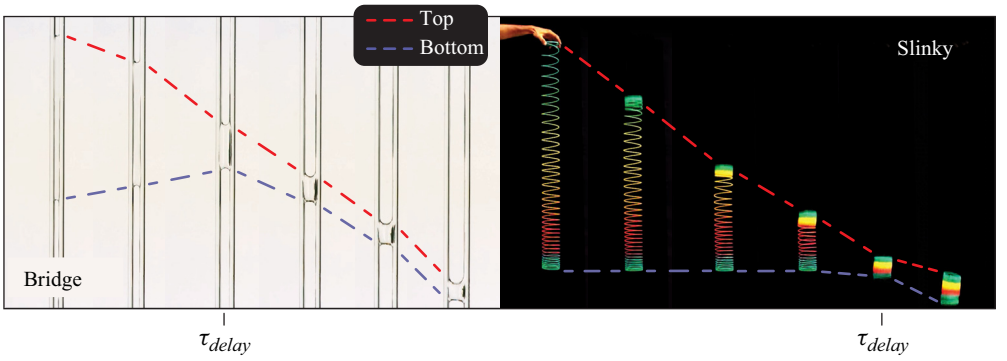

Figure 9. Image sequence of a liquid column between two dry fibres that are being separated at a constant rate shows that the bridge contracts towards its centre of mass and then descends along the fibres due to gravity. For short time $\tau < \tau_{delay}$, the bridge's motion predominantly transitions its shape between column-like and drop-like, after which gravity causes net drop motion. This delay in the onset of descending drop motion is analogous to the dynamic behaviour observed in the 'falling slinky' phenomenon, where a stretched slinky appears to hover momentarily before collapsing.

findings can further advance liquid control and transport between fibres in innovative and bio-inspired systems (Meng *et al.* 2014; Wang *et al.* 2017). Furthermore, flowing liquid between fibres is common in fog collectors, as observed in the laboratory (Shi *et al.* 2018) and in the field (Moncuquet *et al.* 2022). Thus novel geometries for water harvesting (Bintein *et al.* 2023) and materials capable of simultaneously harvesting and cleaning water (Ghosh 2023) offer impactful opportunities for further research. Our findings offer valuable physical insights into flowing liquid bridges, with the potential to advance the current state of the art in these areas.

The study of flow down a fibre has revealed rich physics over the past two decades. Likewise, we expect the study of flow between fibres to provide both practical and physical intrigue. Here, we studied flowing bridges, but the transition from static to dynamic bridges exhibits interesting behaviour yet to be explored. For example, figure 9 shows a liquid bridge held statically between two closely spaced vertical fibres that is put into motion as the fibres are separated at a constant rate. Interestingly, the drop 'floats': its primary motion is inwards, pulling the bottom of the bridge up the fibre, until a critical time τ_{delay} when the bridge succumbs to gravity and falls. This phenomenon shares several qualitative similarities with the classic 'falling slinky' problem, where a stretched spring also appears to float for some short time $t < \tau_{delay}$ before falling (Cross & Wheatland 2012). Thus the intriguing behaviour of falling liquid bridges between fibres offers a fluidic twist on this popular physics demonstration, as shown in movie 5 of the supplementary material. Alternatively, at the high end of possible w values, many aspects of bridge detachment remain unexplored. For example, the role of viscous and capillary forces on the detachment of flowing bridges is worth pursuing, especially since previous works have shown that viscosity plays a critical role in bridge rupture (Mazzone *et al.* 1987). These forces may also be considered for determining the physics underpinning the coating of fibres using bridge patterns via the capillary number Ca, which has long been known to control the coating of many thin structures and flat plates according to the Landau–Levich–Derjaguin law (Levich & Landau 1942; Deriagin & Levi 1964). A better understanding of the film deposited by flowing bridges may also allow them to be functionalized to deposit suspended particulate via capillary deposition, a concept already explored in the laboratory

(Jeong *et al.* 2020) and used to deliver drugs in a circular geometry (Kim *et al.* 2017), but unexplored for fibrous systems. Furthermore, the coating of dry fibres with flowing bridges remains unexplored but is expected to yield valuable physical insight akin to that found for beads coating vertical fibres and fibre bundles (Leonard *et al.* 2023)

Finally, it is worth emphasizing the exceptional degree of control and the myriad of patterns that extend well beyond the scope of what has been highlighted in this paper. For instance, liquid bridges can flow between curved fibres or along a winding trajectory (Gabbard & Bostwick 2023*b*). In these scenarios, liquid bridges can be purposely engineered to glide, twist and traverse intricate paths, necessitating the incorporation of additional physics, such as the interplay between adhesion and liquid weight (Aziz & Tafreshi 2019), which will determine if bridges flow or detach. Furthermore, bridges can flow between arrays of more than two fibres (Gabbard & Bostwick 2023*b*), a scenario that approaches plug flow in a tube as the number of fibres increases. The wealth of potential flow structures and their adaptability presents an ideal canvas for innovative system design, and equips creative practitioners with effective means to craft novel and sophisticated solutions to fluid transport problems.

Supplementary material. Supplementary movies are available at https://doi.org/10.1017/jfm.2024.794.

Funding. J.B.B. acknowledges support from NSF grant CMMI-1935590.

Declaration of interests. The authors report no conflict of interest.

Author ORCIDs.
Joshua B. Bostwick https://orcid.org/0000-0001-7573-2108.

Appendix A. Equilibrium length of a column between parallel fibres

Here, we restate the results for the scaling of static liquid bridges between fibres from Princen (1970) and Protiere *et al.* (2013) for completeness, which we use to compare with our experimental data shown in figures 5(*b*) and 7(*d*).

We begin by considering the force balance on a small volume of fluid in equilibrium between two long, parallel fibres, $\mathrm{d}V = A\,\mathrm{d}L$:

$$4\sigma r\alpha\,\mathrm{d}L - 4\sigma R\left(\frac{\pi}{2}\right)\mathrm{d}L - \sigma\frac{A\,\mathrm{d}L}{R} = 0, \tag{A1}$$

which includes forces at the free surface and fibre–liquid interface, and the force associated with the Laplace pressure in the column σ/R. We define a geometric factor $f(\alpha) = 2\alpha - \sin 2\alpha$, where α is the angle between the line connecting the centre of the fibres and the line from the centre of a fibre to the liquid–solid–vapour contact line. Letting $\tilde{A} = A/r^2$ and $\tilde{R} = R/r$, we can relate $\tilde{A}$ to $\tilde{R}$ and α through

$$\tilde{A} = \tilde{R}^2\,(4\alpha - \pi - f(\alpha)) + 2\tilde{R}\sin 2\alpha - f(\alpha). \tag{A2}$$

The radius of curvature is then given by

$$\tilde{R} = \left(\sqrt{\frac{\pi}{f(\alpha)}} - 1\right)^{-1}, \tag{A3}$$

and we can define the fibre spacing as $\tilde{w} = w/r$ and express it in terms of α and $\tilde{R}$:

$$\tilde{w} = 2(\cos\alpha(1+\tilde{R}) - 1). \tag{A4}$$

The theoretical length of a column is given by (A2)–(A4) since each w gives a unique cross-sectional shape such that $\ell r_f^2/V = 1/\tilde{A}$ as plotted in figures 5(b) and 7(d).

References

Aziz, H. & Tafreshi, H.V. 2019 Competing forces on a liquid bridge between parallel and orthogonal dissimilar fibers. *Soft Matt.* **15** (35), 6967–6977.

Bao, J., Wang, Z., Song, C., Zhang, Y., Li, Z., Zhang, L., Lan, R. & Yang, H. 2023 Shape-programmable liquid crystalline polyurethane-based multi-mode actuators triggered by light-driven molecular motors. *Adv. Mater.* **35**, 2302168.

Bintein, P.-B., Cornu, A., Weyer, F., De Coster, N., Vandewalle, N. & Terwagne, D. 2023 Kirigami fog nets: how strips improve water collection. *npj Clean Water* **6** (1), 54.

Cazaubiel, A. & Carlson, A. 2023 Influence of wind on a viscous liquid film flowing down a thread. *Phys. Rev. Fluids* **8** (5), 054002.

Chen, X., Kornev, K.G., Kamath, Y.K. & Neimark, A.V. 2001 The wicking kinetics of liquid droplets into yarns. *Text. Res. J.* **71** (10), 862–869.

Chinju, H., Uchiyama, K. & Mori, Y.H. 2000 'String-of-beads' flow of liquids on vertical wires for gas absorption. *AIChE J.* **46** (5), 937–945.

Cross, R.C. & Wheatland, M.S. 2012 Modeling a falling slinky. *Am. J. Phys.* **80** (12), 1051–1060.

Deriagin, B.V. & Levi, S.M. 1964 *Film Coating Theory: The Physical Chemistry of Coating Thin Layers on a Moving Support*. Focal.

Duprat, C., Giorgiutti-Dauphiné, F., Tseluiko, D., Saprykin, S. & Kalliadasis, S. 2009 Liquid film coating a fiber as a model system for the formation of bound states in active dispersive-dissipative nonlinear media. *Phys. Rev. Lett.* **103** (23), 234501.

Duprat, C. & Protiere, S. 2015 Capillary stretching of fibers. *Europhys. Lett.* **111** (5), 56006.

Duprat, C., Protiere, S., Beebe, A.Y. & Stone, H.A. 2012 Wetting of flexible fibre arrays. *Nature* **482** (7386), 510–513.

Duprat, C., Ruyer-Quil, C., Kalliadasis, S. & Giorgiutti-Dauphiné, F. 2007 Absolute and convective instabilities of a viscous film flowing down a vertical fiber. *Phys. Rev. Lett.* **98** (24), 244502.

Eghbali, S., Keiser, L., Boujo, E. & Gallaire, F. 2022 Whirling instability of an eccentric coated fibre. *J. Fluid Mech.* **952**, A33.

Entov, V.M. & Hinch, E.J. 1997 Effect of a spectrum of relaxation times on the capillary thinning of a filament of elastic liquid. *J. Non-Newtonian Fluid Mech.* **72** (1), 31–53.

Gabbard, C.T. & Bostwick, J.B. 2021*a* Asymmetric instability in thin-film flow down a fiber. *Phys. Rev. Fluids* **6** (3), 034005.

Gabbard, C.T. & Bostwick, J.B. 2021*b* Scaling analysis of the Plateau–Rayleigh instability in thin film flow down a fiber. *Exp. Fluids* **62** (7), 141.

Gabbard, C.T. & Bostwick, J.B. 2023*a* Bead-on-fibre morphology in shear-thinning flow. *J. Fluid Mech.* **961**, A14.

Gabbard, C.T. & Bostwick, J.B. 2023*b* Thin film flow between fibers: inertial sheets and liquid bridge patterns. *Phys. Rev. Fluids* **8**, 110505.

Gallaire, F. & Brun, P.-T. 2017 Fluid dynamic instabilities: theory and application to pattern forming in complex media. *Phil. Trans. R. Soc.* A **375** (2093), 20160155.

Ghosh, R. 2023 Photocatalytically reactive surfaces for simultaneous water harvesting and treatment. *Nat. Sustainability* **6**, 1663–1672.

Guo, L. & Tang, G.H. 2015 Experimental study on directional motion of a single droplet on cactus spines. *Intl J. Heat Mass Transfer* **84**, 198–202.

Jeong, D.-H., Kvasnickova, A., Boutin, J.-B., Cébron, D. & Sauret, A. 2020 Deposition of a particle-laden film on the inner wall of a tube. *Phys. Rev. Fluids* **5** (11), 114004.

Jin, R., Zheng, H., Zhao, Z., Ma, X., Wang, L., Qi, C. & Kong, H. 2023 A novel thermal desalting process using a binary string-of-beads flow array. *Appl. Therm. Engng* **226**, 120208.

Ju, J., Bai, H., Zheng, Y., Zhao, T., Fang, R. & Jiang, L. 2012 A multi-structural and multi-functional integrated fog collection system in cactus. *Nat. Commun.* **3** (1), 1247.

Kawase, T., Sekoguchi, S., Fuj, T. & Minagawa, M. 1986 Spreading of liquids in textile assemblies. Part I. Capillary spreading of liquids. *Text. Res. J.* **56** (7), 409–414.

Khattak, H.K., Shanzeela, A., Raphael, E. & Dalnoki-Veress, K. 2024 Directed droplet motion along thin fibers. *PNAS Nexus* **3**, pgae086.

KIM, J., GUENTHART, B., O'NEILL, J.D., DORRELLO, N.V., BACCHETTA, M. & VUNJAK-NOVAKOVIC, G. 2017 Controlled delivery and minimally invasive imaging of stem cells in the lung. *Sci. Rep.* **7** (1), 13082.

KISSA, E. 1981 Capillary sorption in fibrous assemblies. *J. Colloid Interface Sci.* **83** (1), 265–272.

KLIAKHANDLER, I.L., DAVIS, S.H. & BANKOFF, S.G. 2001 Viscous beads on vertical fibre. *J. Fluid Mech.* **429**, 381–390.

KURTYIGIT, I.E., GUO, Y., SINGER, J., DEMAURO, E.P. & DRAZER, G. 2023 Inertial capture of aerosol particles using liquid bridges in cross flow. *J. Aerosol Sci.* **175**, 106278.

LABBÉ, R. & DUPRAT, C. 2019 Capturing aerosol droplets with fibers. *Soft Matt.* **15** (35), 6946–6951.

LEONARD, M., VAN HULLE, J., WEYER, F., TERWAGNE, D. & VANDEWALLE, N. 2023 Droplets sliding on single and multiple vertical fibers. *Phys. Rev. Fluids* **8** (10), 103601.

LEVICH, B. & LANDAU, L. 1942 Dragging of a liquid by a moving plate. *Acta Physicochim. URSS* **17**, 42.

LUKÁŠ, D., CHALOUPEK, J., KOŠŤÁKOVÁ, E., PAN, N. & MARTINKOVA, I. 2006 Morphological transitions of capillary rise in a bundle of two and three solid parallel cylinders. *Physica* A **371** (2), 226–248.

MAZZONE, D.N., TARDOS, G.I. & PFEFFER, R. 1987 The behavior of liquid bridges between two relatively moving particles. *Powder Technol.* **51** (1), 71–83.

MENG, Q., WANG, Q., LIU, H. & JIANG, L. 2014 A bio-inspired flexible fiber array with an open radial geometry for highly efficient liquid transfer. *NPG Asia Mater.* **6** (9), e125 .

MIGITA, H., SOGA, K. & MORI, Y.H. 2005 Gas absorption in a wetted-wire column. *AIChE J.* **51** (8), 2190–2198.

MINOR, F.W., SCHWARTZ, A.M., WULKOW, E.A. & BUCKLES, L.C. 1959 The migration of liquids in textile assemblies. Part II. The wicking of liquids in yams. *Text. Res. J.* **29** (12), 931–939.

MONCUQUET, A., MITRANESCU, A., MARCHAND, O.C., RAMANANARIVO, S. & DUPRAT, C. 2022 Collecting fog with vertical fibres: combined laboratory and in-situ study. *Atmos. Res.* **277**, 106312.

MONTANERO, J.M. & PONCE-TORRES, A. 2020 Review on the dynamics of isothermal liquid bridges. *Appl. Mech. Rev.* **72** (1), 010803.

PATNAIK, A., RENGASAMY, R.S., KOTHARI, V.K. & GHOSH, A. 2006 Wetting and wicking in fibrous materials. *Text. Prog.* **38** (1), 1–105.

PITOIS, O., MOUCHERONT, P. & CHATEAU, X. 2000 Liquid bridge between two moving spheres: an experimental study of viscosity effects. *J. Colloid Interface Sci.* **231** (1), 26–31.

PLATEAU, J. 1873 *Statique experimentale et theorique des liquides soumis aux seules forces moleculaires*, vol. 2. Gauthier-Villars.

PRINCEN, H.M. 1970 Capillary phenomena in assemblies of parallel cylinders. III. Liquid columns between horizontal parallel cylinders. *J. Colloid Interface Sci.* **34** (2), 171–184.

PROTIERE, S., DUPRAT, C. & STONE, H.A. 2013 Wetting on two parallel fibers: drop to column transitions. *Soft Matt.* **9** (1), 271–276.

QUÉRÉ, D. 1999 Fluid coating on a fiber. *Annu. Rev. Fluid Mech.* **31** (1), 347–384.

RAYLEIGH, LORD 1878 On the instability of jets. *Proc. Lond. Math. Soc.* **1** (1), 4–13.

SADEGHPOUR, A., OROUMIYEH, F., ZHU, Y., KO, D.D., JI, H., BERTOZZI, A.L. & JU, Y.S. 2021 Experimental study of a string-based counterflow wet electrostatic precipitator for collection of fine and ultrafine particles. *J. Air Waste Manage. Assoc.* **71** (7), 851–865.

SADEGHPOUR, A., ZENG, Z., JI, H., DEHDARI EBRAHIMI, N., BERTOZZI, A.L. & JU, Y.S. 2019 Water vapor capturing using an array of traveling liquid beads for desalination and water treatment. *Sci. Adv.* **5** (4), eaav7662.

SAURET, A., BOULOGNE, F., CÉBRON, D., DRESSAIRE, E. & STONE, H.A. 2015*a* Wetting morphologies on an array of fibers of different radii. *Soft Matt.* **11** (20), 4034–4040.

SAURET, A., BOULOGNE, F., SOH, B., DRESSAIRE, E. & STONE, H.A. 2015*b* Wetting morphologies on randomly oriented fibers. *Eur. Phys. J.* E **38**, 1–9.

SHI, W., ANDERSON, M.J., TULKOFF, J.B., KENNEDY, B.S. & BOREYKO, J.B. 2018 Fog harvesting with harps. *ACS Appl. Mater. Interfaces* **10** (14), 11979–11986.

SHI, W., DE KONINCK, L.H., HART, B.J., KOWALSKI, N.G., FUGARO, A.P., VAN DER SLOOT, T.W., OTT, R.S., KENNEDY, B.S. & BOREYKO, J.B. 2020 Harps under heavy fog conditions: superior to meshes but prone to tangling. *ACS Appl. Mater. Interfaces* **12** (42), 48124–48132.

SRIDHAR, T., TIRTAATMADJA, V., NGUYEN, D.A. & GUPTA, R.K. 1991 Measurement of extensional viscosity of polymer solutions. *J. Non-Newtonian Fluid Mech.* **40** (3), 271–280.

TER HAAR, D. 2016 *Collected Papers of P.L. Kapitza: USSR Academy of Sciences, FRS*, vol. 1. Elsevier.

WAGSTAFF, C., GUBBA, S.R., TRUSCOTT, T., ALGASHGARI, K. & ROBERTS, W.L. 2023 Wire density for a wetted-wire column. *Chem. Engng Sci.* **273**, 118633.

WANG, F. & SCHILLER, U.D. 2021 Hysteresis in spreading and retraction of liquid droplets on parallel fiber rails. *Soft Matt.* **17** (22), 5486–5498.

WANG, P., BIAN, R., MENG, Q., LIU, H. & JIANG, L. 2017 Bioinspired dynamic wetting on multiple fibers. *Adv. Mater.* **29** (45), 1703042.

WILSON, J.L., PAHLAVAN, A.A., ERININ, M.A., DUPRAT, C., DEIKE, L. & STONE, H.A. 2023 Aerodynamic interactions of drops on parallel fibres. *Nat. Phys.* **19**, 1667–1672.

XUE, Y., WANG, T., SHI, W., SUN, L. & ZHENG, Y. 2014 Water collection abilities of green bristlegrass bristle. *RSC Adv.* **4** (77), 40837–40840.

ZENG, Z., SADEGHPOUR, A. & JU, Y.S. 2019 A highly effective multi-string humidifier with a low gas stream pressure drop for desalination. *Desalination* **449**, 92–100.

ZENG, Z., SADEGHPOUR, A., WARRIER, G. & JU, Y.S. 2017 Experimental study of heat transfer between thin liquid films flowing down a vertical string in the Rayleigh–Plateau instability regime and a counterflowing gas stream. *Intl J. Heat Mass Transfer* **108**, 830–840.

ZHENG, Y., BAI, H., HUANG, Z., TIAN, X., NIE, F.-Q., ZHAO, Y., ZHAI, J. & JIANG, L. 2010 Directional water collection on wetted spider silk. *Nature* **463** (7281), 640–643.